

Vacancy-Engineered Phonon Polaritons in α -MoO₃

Naveed Hussain,¹ Mashnoon Alam Sakib,¹ Zhaoxu Li,² William Harris,^{1,3} Shehzad

Ahmed,⁴ Ruqian Wu,³ H. Kumar Wickramasinghe,^{1,2} Maxim R. Shcherbakov^{1,2,5}

¹*Department of Electrical Engineering and Computer Science, University of California, Irvine, CA 92697*

²*Department of Materials Science and Engineering, University of California, Irvine, CA 92697*

³*Department of Physics, University of California, Irvine, CA 92697*

⁴*College of Physics and Optoelectronic Engineering, Shenzhen University, Guangdong 518060, P. R China*

⁵*Beckman Laser Institute and Medical Clinic, University of California, Irvine, CA 92612*

Low-symmetry van der Waals (vdW) materials have enabled strong confinement of mid-infrared light through hyperbolic phonon polaritons (HPhPs) at the nanoscale. Yet, the bottleneck persists in manipulating the intrinsic polaritonic dispersion to drive further progress in phonon-polaritonics. Here, we present a thermomechanical strategy to manipulate HPhPs in α -MoO₃ using high pressure and temperature treatment. The hot pressing engineers the stoichiometry of α -MoO₃ by controllably introducing oxygen vacancy defects (OVDs), which cause a semiconductor-to-semimetal transition. Our density functional theory (DFT) and finite-difference time-domain (FDTD) results, combined with experimental studies show that the OVDs induce a metastable metallic state by reducing the bandgap, while modifying the intrinsic dielectric permittivity of α -MoO₃. Photo-induced force microscopy (PiFM) confirms an average dielectric permittivity tunability of $|\Delta\varepsilon/\varepsilon| \approx 0.35$ within a Reststrahlen band of α -MoO₃, resulting in drastic shifts in the HPhP dispersion. The polariton lifetimes for pristine

and hot-pressed flakes were measured as 0.92 ± 0.06 and 0.86 ± 0.11 ps, respectively, exhibiting a loss of only 7%, while the group velocity exhibited an increase of $38.8 \pm 0.2\%$. The OVDs in α -MoO₃ provide a low-loss platform that enables active tuning of mid-infrared HPhPs and have a profound impact on applications in super-resolution imaging, nanoscale thermal manipulation, boosted molecular sensing, and on-chip photonic circuits.

Keywords: *Hot-pressing, Stoichiometry Engineering, Oxygen Vacancy Defects, Hyperbolic Phonon Polaritons (HPhPs), Photoinduced Force Microscopy (PiFM), α -MoO₃.*

Hyperbolic phonon polaritons (HPhPs) are quasi-particles in anisotropic polar crystals merging from the coupling of light and optical phonons. They are ideal candidates for electrooptical modulation, light transmission, sub-diffraction imaging, and molecular detection due to their strong field confinement, low loss, and long lifetimes.¹⁻⁵ Controlling HPhPs is desired for nanoscale light manipulation, enabling significant advancements in nanophotonics. However, the lack of external control to manipulate HPhPs in most polar crystals, likely due to their large bandgap window (2 to 10 eV), hinders their applicability.⁶ Substantial efforts have been made to manipulate HPhPs in various material systems, including subwavelength metallic and hyperbolic metamaterials,⁷⁻⁹ and dielectric photonic crystals.¹⁰⁻¹² Two-dimensional (2D) van der Waals (vdW) layered polar crystals have provided an additional degree of freedom in controlling light over a wide spectral range. Attempts were made to alter the dielectric environment by fabricating out-of-plane heterostructures of vdW crystals such as hexagonal boron nitride (h-BN)/black phosphorous¹³ and MoS₂/SiC¹⁴ combining polaritonic metasurfaces, phase change materials,¹⁵⁻¹⁷ and by suspending polar materials in air.¹⁸ However, the excessive spatial confinement

of polaritons owing to the reflection and scattering losses inherent to such crystals render it hard to manipulate their HPhPs dispersion, particularly in mid-infrared region.¹⁹

α -MoO₃ is an exciting low-symmetry vdW semiconductor that enables strongly confined hyperbolic dispersion in the mid-infrared due to its ultra-low-loss and in-plane anisotropic HPhPs.^{20,21} The extreme sensitivity of α -MoO₃ towards its physical and chemical properties allows effective tuning of HPhP propagation. For instance, electron doping and intercalation of metal atoms like Co and Sn into the lattice interlayers can modify the HPhP characteristics.^{22,23} The reversible intercalation of hydrogen atoms to manipulate HPhPs in α -MoO₃ has also been presented.⁶ However, incorporating foreign atoms as dopants or intercalators into the crystal lattice of α -MoO₃ inhibits its intrinsic hyperbolic dispersion, primarily due to the solution-processing techniques and the subsequent increase in volume, resulting in significant losses in polariton lifetimes (τ).

To our knowledge, stoichiometry engineering as an alternative approach to manipulating the HPhPs in α -MoO₃ by exploiting controlled oxygen vacancy defects to alter its intrinsic dielectric permittivity (ϵ) has not been practically achieved. The stoichiometry of α -MoO₃ varies strongly with the oxygen vacancy defects (OVDs); with a wide bandgap (>2.7 eV) and Mo⁶⁺ valance state, to intermediate reduced oxides (MoO_{3-x}, $0 < x < 1$), to semimetallic MoO₂ with an oxidation state of Mo⁴⁺.²⁴ Such composition in α -MoO₃ may modify ϵ , thereby, providing an unprecedented opportunity to control and manipulate its HPhPs dispersion on demand.

Here, we demonstrate a thermomechanical approach to tune the hyperbolic phonon polariton response in α -MoO₃ by engineering its stoichiometry through a controlled introduction of OVDs. Exfoliated α -MoO₃ flakes were placed between silicon substrates and hot-pressed at

temperatures up to 400 °C, with step increments of 50 °C, applying a high uniaxial pressure (~0.1–0.2 GPa). This process ensures limited oxygen supply, which is necessary to induce oxygen vacancy defects (OVDs). The application of uniaxial pressure facilitated maximum strain transfer through the interfacial in-plane coefficient of thermal expansion (CTE) mismatch, inducing a controlled biaxial compressive strain up to –2.4%. This strain and the introduction of OVDs were confirmed by μ -Raman spectroscopy, while the chemical stoichiometry was confirmed by X-ray photoelectron spectroscopy (XPS). Our density functional theory (DFT) calculation and photoluminescence and chemical stoichiometry experiments confirmed the semiconductor (α -MoO₃) to a stable semi-metallic/metallic MoO_{3-x} transition with the introduction of OVDs. The DFT calculations also validated alterations in the dielectric characteristics of α -MoO₃ due to the presence of OVDs. This permitted significant engineering in the HPhPs dispersion in a hot-pressed (*h.p.*) nanoflake compared to the pristine sample, as measured by the photo-induced force microscopy (PiFM) technique. The outcomes were consistent with our model, which incorporated finite-difference time-domain (FDTD) simulations and experimental PiFM data, showing an extraordinary dielectric permittivity modulation of up to $|\Delta\varepsilon/\varepsilon| \approx 0.35$. We believe that hot-pressing-induced engineering of phonon modes in α -MoO₃, and the introduction of OVDs provide essential control over mid-infrared HPhPs. Hot-pressed α -MoO₃ shows great promise for nanophotonic applications, including super-resolution imaging, nanoscale thermal manipulation, enhanced molecular sensing, and on-chip optical circuitry.

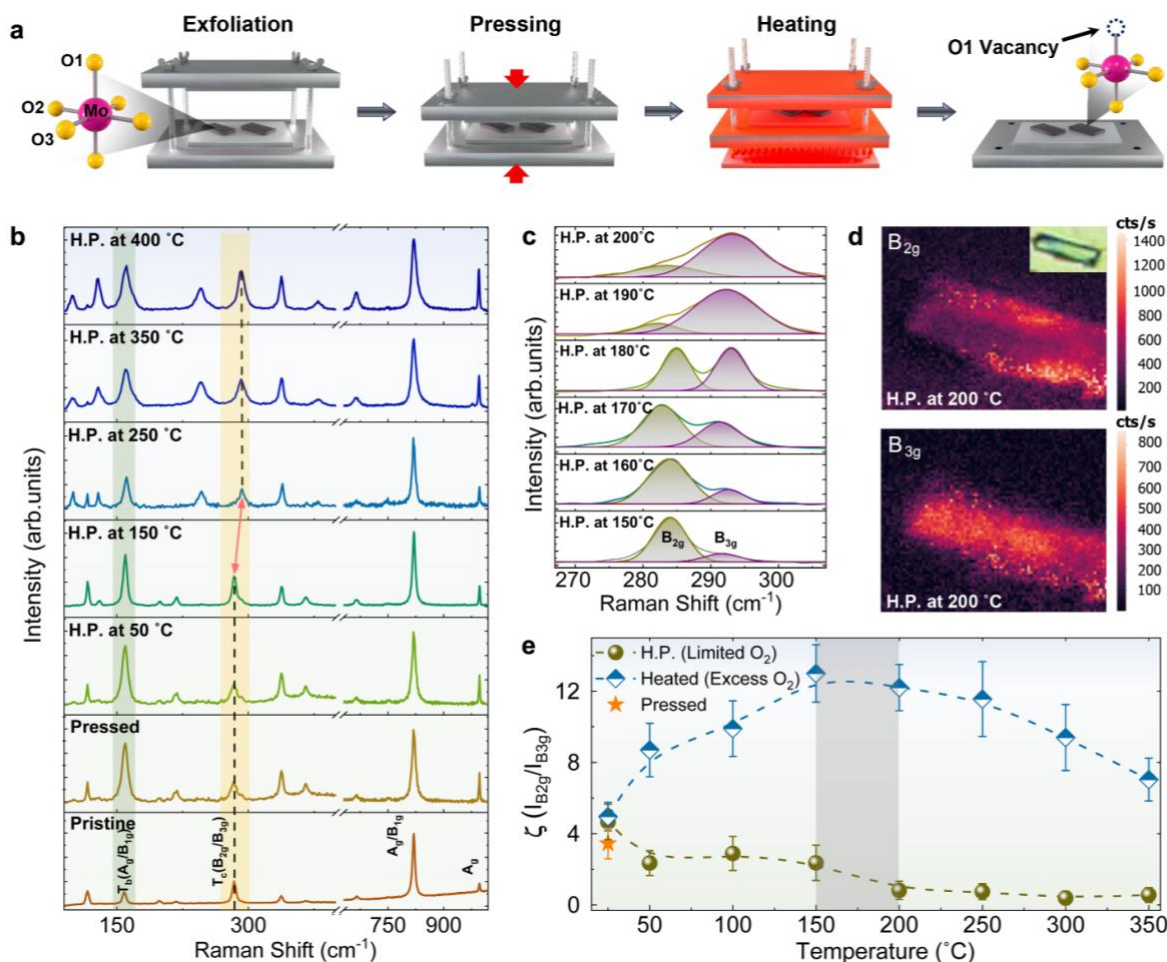


Figure 1. Tunable phononics in thermomechanically processed MoO₃. **a**, Schematic illustration of thermomechanical processing of α -MoO₃ flakes using hot-pressing technique. Each Mo atom is coupled with three oxygen atoms, i.e., O1, O2 and O3, representing terminal oxygens, doubly coordinated bridging oxygens and triply coordinated oxygens, respectively. **b**, μ -Raman spectra of the pristine, pressed and *h.p.* α -MoO₃ at 50, 150, 250, 350, and 400 °C, with T_b and T_c mode highlighted in green and yellow, respectively. **c**, Magnified Raman spectra (normalized) of T_c (B_{2g}/B_{3g}) mode acquired by h.p. α -MoO₃ from 150 to 200 °C to monitor band transition, representing a decrease in oxygen-to-metal ratio, highlighted by orange double arrow in **b**. **d**, Raman intensity maps of the nanoflake h.p. at 200 °C, constructed by B_{2g} (at 284 cm⁻¹, top) and B_{3g} (at 291 cm⁻¹, bottom) modes. **e**, Variation in $\xi = I_{B_{2g}}/I_{B_{3g}}$ of just heated (excess O₂) and *h.p.* (limited O₂) α -MoO₃, showing strikingly dissimilar behaviors.

RESULTS

Thermomechanical Processing and μ -Raman characterization of α -MoO₃ flakes Hot-press synthesis has emerged as a versatile thermomechanical method capable of synthesizing ultrathin 2D crystals and introducing intrinsic defects.^{25,26} We use hot-pressing for the first time to introduce oxygen vacancy defects (OVDs) in mechanically exfoliated α -MoO₃ flakes. The α -MoO₃ flakes were mechanically exfoliated onto a silicon substrate, which was subsequently capped with an identical substrate. The assembly was then inserted in a pressure device assembly (PDA) consisting of steel bars to generate controllable and localized uniaxial pressure (0.1–0.2 GPa) via the top substrate. The uniaxial pressure exerted by the PDA was crucial for cutting off oxygen supply during heating, creating OVDs. Additionally, it ensured strong interfacial adhesion during the relative thermal expansion and contraction processes, offering maximum strain transfer (see [Supporting Information for pressure calculations](#)). Initially, the PDA applied pressure to the flakes, and then the samples were heated in a muffle furnace. In total, eight samples were fabricated, each heated in increments of 50 °C from room temperature (T_r) to 400 °C, while maintaining the same uniaxial pressure. The schematic illustration of thermomechanical processing of α -MoO₃ flakes is shown in [Fig. 1a](#). The field emission scanning electron microscopy (FESEM) images of the flake prior to hot-pressing, the typical PDA, and the flake after hot-pressing have been presented in [Supporting Information, Fig. S1](#).

We performed comprehensive μ -Raman spectroscopy to investigate thermomechanical engineering in phonon modes, resulting in OVDs creation and lattice straining. [Figure 1b](#) shows the μ -Raman spectra of pristine, pressed, and hot-pressed flakes in a muffle furnace under ambient conditions at 50, 100, 150, 250, 350, and 400 °C. The spectrum revealed vibrational bands that correspond to the stretching modes between 1000 and 600 cm⁻¹,

deformation modes between 600 and 400 cm^{-1} , and lattice modes below 200 cm^{-1} . All samples displayed distinct and robust bands at 117, 129, 245, 284, 291, 338, 338, 665, 819, and 996 cm^{-1} . A typical α - MoO_3 (orthorhombic) crystal comprises of a double layer of linked and deformed MoO_6 octahedra and is thermodynamically stable. The relatively weak peak at 996 cm^{-1} is the A_g mode attributed to the asymmetric $\text{Mo}^{6+}=\text{O}_{(1)}$ stretching mode of terminal oxygen along the b-axis. The band at 819 cm^{-1} is the most intense (ν_s) band that corresponds to the symmetric stretching mode of doubly coordinated oxygen ($\text{Mo}_2\text{-O}_{(3)}$), which originates from the oxygen shared by the two MoO_6 octahedra and is sensitive to oxygen vacancies and defects.²⁷ The full width at half maximum (FWHM) of this peak provides crucial information regarding the presence of OVDs in α - MoO_3 flakes. The peak broadens as hot-pressing temperature increases, with the FWHM increasing from 8.2 cm^{-1} for pristine to 15.12 cm^{-1} for flakes *h.p.* at 350 °C; see [Supporting Information Fig. S2](#). This inhomogeneous peak broadening is the result of a decrease in the lifetime of excited states, which is typically driven by an increase in the concentration of OVDs, i.e. a significant decrease in the oxygen-to-metal ratio.²⁸ Probing the engineering in T_b (A_g/B_{1g}), the translational chain mode at 158.4 cm^{-1} is critical in determining the lattice strain, while the T_c (B_{2g}/B_{3g}) mode comprising of 284 cm^{-1} (B_{2g}) and its shoulder at 291 cm^{-1} (B_{3g}) is crucial in assessment of OVDs. Results show that the hot-pressing engineers the phonon modes related to lattice and valance state, introducing OVDs and lattice strain in α - MoO_3 .

The oxygen vacancies in α - MoO_3 can be detected by variation in the ratio of intensities of B_{2g} (at 284 cm^{-1}), and B_{3g} (at 291 cm^{-1}) Raman modes i.e., $\xi = I_{B_{2g}}/I_{B_{3g}}$.^{29,30} In pristine α - MoO_3 , the intensity of the shoulder peak ($I_{B_{3g}}$) of T_c phonon mode at 291 cm^{-1} was weak, which corresponds to the least oxygen vacancies. A consistent increase was observed in $I_{B_{3g}}$ for pressed, 50, 100, and 150 °C *h.p.* flakes, which indicated a steady increase in OVDs.

Intriguingly, for samples hot-pressed at temperatures of 200 °C or higher, we observed a complete crossover in intensities of B_{2g} and B_{3g} modes, where $I_{B_{3g}}$ became the primary mode while $I_{B_{2g}}$ converted to the shoulder, indicating a dramatic increase in OVDs, highlighted in Fig. 1b by the orange arrow. To carefully investigate this cross-over, we prepared samples with hot-pressing temperatures of 160, 170, 180, and 190 °C and performed μ -Raman investigations, as shown in Fig. 1c. The complete crossover between $I_{B_{3g}}$ and $I_{B_{2g}}$ took place between h.p. temperature of 150 and 200 °C took place at 180 °C, making it the cross-over point. The intensity of the B_{3g} mode, however, continued to steadily increase with increasing *h.p.* temperature until it reached saturation at 300 °C. Therefore, the controllable induction of OVDs through hot-pressing is confirmed. The image at the top in Fig. 1d shows the intensity distribution of B_{2g} Raman mode (at 284 cm⁻¹), typically associated with oxygen content indicated the loss of oxygen concentrated primarily at the center of the flake. The inset shows the optical micrograph of the mapped flake. The bottom image displays the intensity distribution of B_{3g} Raman mode (at 291 cm⁻¹), attributed to the Mo content revealed strong intensity, showing the relative increase in Mo content, confirming our hypothesis.

It was crucial to compare our results with just heated samples (without uniaxial pressure by the identical substrate) to determine the effects of hot-pressing on oxygen content (Fig. 1d). We observed a remarkable contrast in the oxygen to molybdenum ratio ξ for heated and *h.p.* samples. The heated flakes exhibited an increase in ξ from the factor of 4.5 for pristine to a maximum of 13 at 200 °C before dropping to 7 at 350 °C. However, ξ decreased by an order of a magnitude from 4.5 for pristine to 0.45 for the flake *h.p.* at 350 °C. It should be noted that this cannot provide an exact quantification of oxidation states and OVDs in *h.p.* flakes and that this requires an independent investigation to accomplish.³⁰ Nevertheless, the results confirmed the possibility of introducing terminal oxygen vacancy (t-O₁) defects in a

controlled manner by hot-pressing α -MoO₃ flakes at varying temperatures, which alters its stoichiometry.

To understand which site contributes the most to the thermally induced OVDs, it is important to understand the inter- and intralayer contributions to the phonons in α -MoO₃. In a typical α -MoO₃ crystal, each Mo atom is bonded to three inequivalent oxygen atoms O₁, O₂, and O₃. The O₁ is often termed as the terminal oxygen (t-O₁), owing to its proximity to the vdW gaps and larger bond lengths, have the least stretching force constants ($f_{16} = 9.3$ N/m, and $f_{17} = 2$ N/m) compared to the force constants along the interchain and intrachain directions.³¹ This allows t-O₁ to lose its bond with Mo at a minimal supply of energy, making it the primary contributor in the creation of OVDs. Their proximity to vdW gaps further facilitates their escape from α -MoO₃ crystal, leaving the vacancies at O₁ site.

Lattice Strain Estimation It was rational to anticipate the lattice strain within *h.p.* flakes, (as shown [Supporting Information, Figure 3](#)), as there is a strong correlation between oxygen vacancies and lattice strain in transition metal oxides.^{33,34} [Fig. S3a](#) shows a consistent blue shift in T_b mode originally located at 158.4 cm⁻¹, for samples hot-pressed up to 350 °C before relaxing back to its position at 400 °C. The amount of strain and its type were calculated as $\delta(\%) = (\omega_{T_b}(\text{pristine}) - \omega_{T_b}(\text{h.p.})) / (\omega_{T_b}(\text{pristine})) \times 100$, where $\omega_{T_b}(\text{pristine})$ and $\omega_{T_b}(\text{h.p.})$ are the frequencies of the T_b phonon mode corresponding to pristine and hot-pressed α -MoO₃, respectively. We attribute the T_b shift to the compressive strain caused by the CTE mismatch at the interface between silicon and α -MoO₃, while the relaxation is caused by the slippage that supersedes the interfacial adhesion above 350 °C. Because the substrate transfers compressive strain, boosting interlayer adhesion between the silicon substrate and α -MoO₃ flakes owing to uniaxial pressure from the top substrate is critical. To

study the impact of uniaxial pressure on compressive strain, we additionally examined heated samples without any uniaxial pressure from the upper substrate. Fig. S3b shows the estimated compressive strain values for hot-pressed (dark green) and bare heated samples (navy). In bare heated samples, the lack of uniaxial pressure results in interfacial slippage at approximately 250°C, which restricted the maximum strain transfer to -1.2% due to the relative CTE approaches. In contrast, interfacial slippage in hot-pressed samples was observed at elevated temperatures (350 °C), resulting in a two-fold increase in maximum strain transfer (-2.4%). We believe that the strain observed in the lattice is not only due to the CTE mismatch but also originates from the introduction OVDs, which our DFT calculations uncovered, as explained later in the paper.

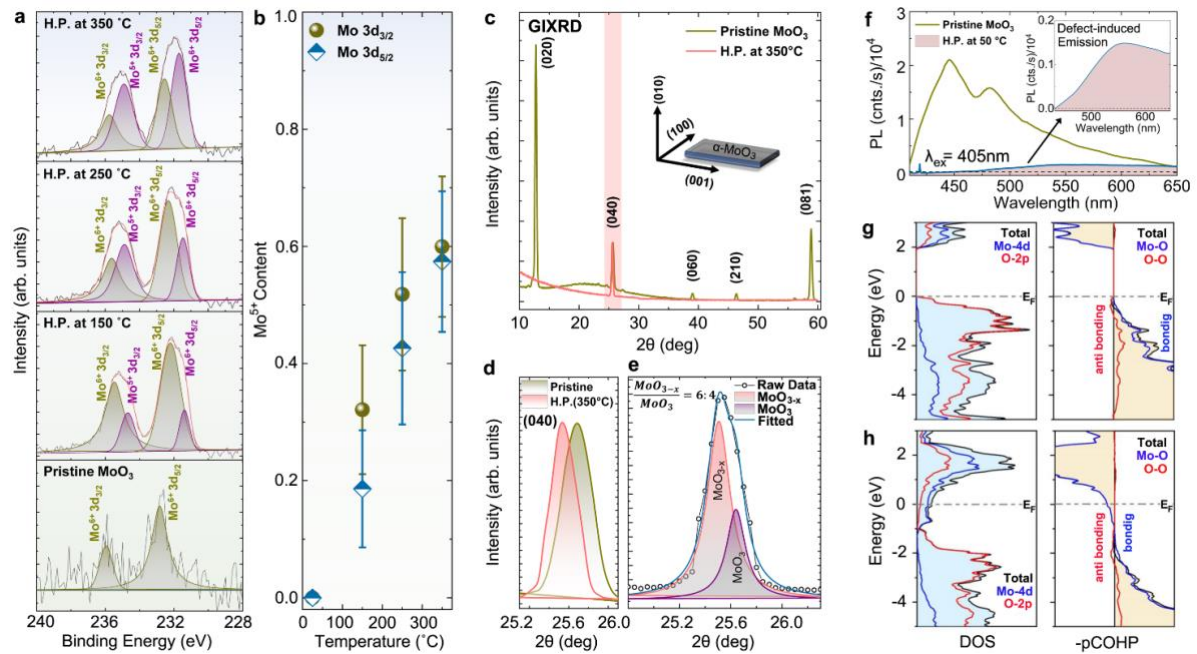


Figure 2. Stoichiometry and electronic band gap characterizations. **a**, Mo3d scan of pristine, and *h.p.* flakes at 150, 250, and 350°C, obtained from XPS investigations to probe the stoichiometry of α - MoO_3 . **b**, Mo^{5+} content in α - MoO_3 , calculated using peak area fitting of $\text{Mo}^{5+}3d_{3/2}$ and $\text{Mo}^{5+}3d_{5/2}$ peaks. **c** GIXRD pattern of the pristine, and *h.p.* α - MoO_3 at 350°C. The inset shows the crystal orientation

of a typical belt-like α -MoO₃ flake. **d**, Comparison of the (040) diffraction peak (normalized) of pristine and h.p. α -MoO₃ at 350, showing a shift by 0.4°. **e**, Deconvolution of (040) diffraction peak of h.p. MoO₃ yields MoO_{3-x} and MoO₃. Peak fitting was performed using the Gaussian function. **f**, Photoluminescence spectra of pristine and h.p. α -MoO₃ at 50°C, using the excitation laser of 405 nm. The inset shows the OVDs-induced PL signal from the h.p. flake. **g**, Total Mo 4d and O 2p density of states and the crystal Orbital Hamilton Population (COHP) analysis partitioned by pairwise interactions of α -MoO₃. **h**, Total Mo 4d and O 2p density of states and the crystal Orbital Hamilton Population (COHP) analysis partitioned by pairwise interactions of MoO_{3-x}. The Fermi level (E_F) is aligned to 0 eV.

Chemical Stoichiometry Studies X-ray photoelectron spectroscopy (XPS) was employed to identify the stoichiometry of pristine and hot-pressed α -MoO₃. The Mo 3d scans of pristine, hot-pressed at 150, and 350 °C samples are shown in [Fig. 2a](#). For pristine α -MoO₃, Mo 3d_{3/2} and Mo 3d_{5/2} are located at binding energies of 235.92 and 232.82 eV, respectively, which corresponds to pure MoO₃ stoichiometry with Mo⁶⁺ oxidation state with hexavalent formal molybdenum ions.^{32,35} Nonetheless, as the temperature rose from 25 to 350°C, the h.p. flakes demonstrated a gradual rise in the proportion of the Mo⁵⁺ state (identified by purple peaks). This indicated a shift in the composition towards a lower oxidation state (MoO_{3-x}). The calculations based on fitted peak areas revealed that the h.p. flakes represented a hybrid system, with the Mo⁵⁺ content in MoO_{3-x} increasing from 0% at 25 °C to approximately 60% for the flakes hot-pressed at 350°C ([Fig. 2b](#)).

In transition metal oxides, the introduction of OVDs also results in increasing the electrical conductivity by an order of a magnitude, as the oxygen vacancies serve as shallow donors which improve carrier mobility.^{36,37} The XPS results complement the Raman results and suggest that the chemical stoichiometry can be controlled by the introduction of OVDs with

increasing *h.p.* temperature. The results also suggested that the increase in OVDs with increase in *h.p.* temperature drives α -MoO₃ from semiconductor to semimetallic state.³⁵ The XPS survey spectrum of α -MoO₃ hot pressed on gold coated Si substrate has been shown in [Supporting Information, Fig. S4](#). The gold-coated substrate was used to obtain a conductive surface for better signal acquisition during XPS experiments.

XRD and EDS Results Grazing angle incident x-ray diffraction (GIXRD) experiments were performed to quantify the transition from pristine α -MoO₃ to reduced α -MoO_{3-x} in hot-pressed flakes. The results in [Fig. 2c](#) indicate the transition from polycrystalline to monocrystalline phase in *h.p.* flakes as there were no peak other than (040) along the basal plane at 25.53°, compared to its pristine counterpart. However, [Fig. 2d](#) shows a shift of 0.4° in (040) peak, which indicates the existence of MoO_{3-x}, and is consistent with previous reports.^{38,39} The peak fitting using Gaussian function was performed and the peak area analysis suggested that the MoO_{3-x}: MoO₃ in a 350°C *h.p.* flake was 6:4 ([Fig. 2e](#)). The results are in striking agreement with that of our XPS results, which confirm a partial reduction of α -MoO₃ (Mo⁶⁺) to α -MoO_{3-x} (Mo⁵⁺). Elemental diffraction spectroscopy (EDS) was performed to confirm the loss of oxygen in *h.p.* α -MoO₃. The EDS mapping results presented in [Supporting Information, Fig. S5](#) affirmed the loss of oxygen in 350°C *h.p.* flakes, where Mo counts were approximately 30% higher than those of oxygen.

Photoluminescence confirmation of semiconductor-to-semimetal transition We performed micro-photoluminescence (μ -PL) studies over the pristine and *h.p.* flakes at 50, 150 and 350°C, using 405 nm laser excitation ([Fig. 2d](#)) to understand the effects of OVDs on the band structure of α -MoO₃. A strong PL signal (peaking at ~2.8 eV) from pristine flake was observed which indicated its semiconducting nature, while there was no significant PL signal from the *h.p.* flakes was observed. Nevertheless, the PL from *h.p.* flakes exhibited a

weak but broad PL signal (highlighted in red), which is presented in the inset and is solely attributed to the defect-induced emission. This provided strong evidence of the semiconductor to semi-metallic transition with the introduction of even a slight amount of OVDs in α -MoO₃.

Electronic density of states (DOS) calculations In a stoichiometric α -MoO₃ crystal, the bandgap typically exists, however, the introduction of oxygen vacancies creates defect states within the bandgap region. These defect states serve as extra energy levels that electrons can occupy, exerting a considerable impact on the electronic characteristics of α -MoO₃. (Supporting Information, Fig. S6a-b). The vacancies occupy electronic states within the bandgap region, impacting the electronic properties of the α -MoO₃ as shown in Supporting Information, Fig. S6c-e, where DOS plots of pristine, and oxygen-deficient (8% and 16%) α -MoO₃ are given. In α -MoO₃ crystal structure, the presence of oxygen vacancies induces a transition to a metastable phase.^{40,41} Crystal Orbital Hamiltonian Population (COHP) was used to explore the electronic interactions and bonding nature between the atoms involved. The COHP analysis examines the bonding interactions and the changes caused by the oxygen vacancies. α MoO₃ exhibits antibonding COHPs below the Fermi level (E_F), especially for the bond types of Mo-O Fig. 2g-h. With the presence of oxygen vacancies, the antibonding COHPs below E_F become pronounced, influencing the electronic structure.^{42,43} This implies that the electronic states involved in the bonding interactions are affected, and the changes induced by the vacancies lead to the formation of a metastable phase in α -MoO₃.

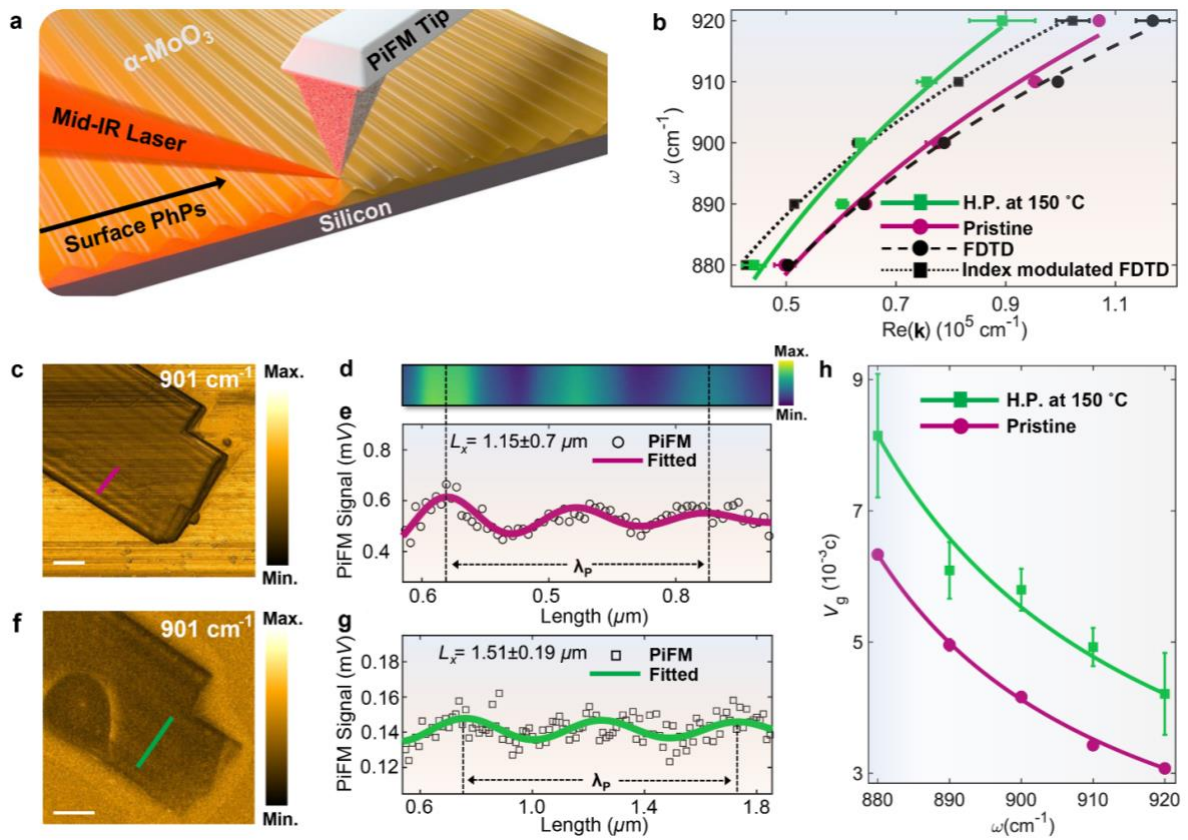


Figure 3. Hyperbolic phonon polariton (HPhP) characterization of pristine and *h.p.* α -MoO₃ using PiFM. **a**, Schematic illustration of measurements of edge-launched HPhPs propagation in α -MoO₃ on silicon substrate using the PiFM technique. **b**, Comparative HPhP dispersion curves of pristine and *h.p.* α -MoO₃ at 150°C. The dashed curves represent the FDTD simulation curves of pristine and refractive index modulated α -MoO₃. **c**, PiFM signal image (901 cm⁻¹) of a 106 ± 1.5 nm thick pristine α -MoO₃ on a Si substrate. The scale bar is 1 μm. **d**, FDTD simulation of HPhPs propagation in pristine α -MoO₃, which matches well with the experiment. **e**, PiFM extracted near-field line trace (circles) and fitted curve (solid line) of pristine α -MoO₃ at 901 cm⁻¹. **f**, PiFM signal image (901 cm⁻¹) of a 107 ± 2 nm thick *h.p.* α -MoO₃ on a Si substrate. The scale bar is 1 μm. **g**, PiFM extracted near-field line trace (squares) and fitted curve (solid line) of 150°C *h.p.* α -MoO₃ at 901 cm⁻¹. **h**, Group velocities (v_g) of HPhPs in pristine and 150°C *h.p.* α -MoO₃ extracted from the fitting results in **b**. The error bars of lifetimes were calculated based on the errors of propagation

lengths originating from the standard deviation of fitting. Measurements were performed in lower Reststrahlen band (L-RB) of α -MoO₃, ranging from 818 to 974 cm⁻¹.

Controlling Surface Phonon-polaritons with OVD Engineering To map the HPhP modes and their modulation in thermomechanically treated α -MoO₃ slabs, hyperspectral photo-induced force microscopy (PiFM) was employed. PiFM uses a pulsed laser source to mechanically detect the gradient of the near-field optical force on the metal-coated AFM tip (Fig. 3a).^{44,45} A cooled mid-infrared detector is not required since the mode of detection is entirely optomechanical, and an image of the z component of the field is produced, which has the same distribution as the local charge density according to Gauss' law. PiFM can acquire hyperspectral images, capturing all resonant modes within the Reststrahlen band of interest from 818 to 974 cm⁻¹. In this region, HPhPs have been shown to propagate along the [100] direction with edge-launched planar wavefronts.⁶

As a proof of concept, we compared pristine and 150 °C *h.p.* flake using the PiFM. The field amplitude images of a pristine ($d = 106 \pm 1.5$ nm), and 150 °C *h.p.* ($d = 107 \pm 2$ nm) α -MoO₃, acquired using PiFM at an excitation frequency of $\omega_0 = 901$ cm⁻¹ have been shown in Fig. 3b,c. Considering the thickness-dependent nature of the HPhP dispersion in α -MoO₃, meticulous attention was given to achieving comparable thicknesses for both pristine and *h.p.* flakes. Atomic force microscopy (AFM) images and the corresponding height profiles of a pristine and a 150 °C *h.p.* flake have been shown in Supporting Information, Fig. S7. The bulge in the middle of the *h.p.* flake (Fig. 3c) is caused by the surface adhesion of the top substrate during the hot-pressing. Despite the same excitation frequency and flake thickness, a clear amplitude damping of the in-plane anisotropic HPhPs along [100] throughout *h.p.* flake is evident, compared to its pristine counterpart, which is attributed to an increased OVD content. However, to fully understand the OVD-mediated modulations in the individual

parameters of in-plane anisotropic HPhPs, such as polariton wavelength (λ_p), propagation lengths (L), group velocity (v_g) and the propagation lifetimes (τ), we extracted the corresponding real-part near-field line scans and fitting curves (solid lines) at 890 cm^{-1} . The line scans highlighted in purple in Fig. 3c and green in Fig. 3f are presented in Fig. 3e and g, respectively. The HPhP propagation length L for pristine and *h.p.* flakes were estimated to be $1.15 \pm 0.07 \mu\text{m}$ and $1.51 \pm 0.19 \mu\text{m}$, respectively. We plotted a comparative dispersion $\omega[\text{Re}(k_x)]$ (where k_x is the complex valued wavevector and x corresponds to the [100] crystal orientation), extracted by fitting the line scans obtained from PiFM images using the function $y = y_0 + Ae^{-\frac{x}{t_0}} \sin\left[\pi\left(\frac{x-x_c}{w}\right)\right]$, where $A, w, t_0 > 0$. Fig. 3e shows the HPhP dispersion curves obtained from the finite difference time domain (FDTD) modelling (dashed curve) using the dielectric permittivity model of $\alpha\text{-MoO}_3$ (Supporting Information, Fig. S8 and Note S2), and the experimentally measured data (solid curve) from PiFM for pristine and *h.p.* flakes. The information extracted from the dispersion curves (Fig. 3f) suggests that the slope of the PiFM measured (solid) and modelled (dashed) curves were similar ($\sim 3.2\%$ average deviation), validating our model. However, a marked difference in the slope of the dispersion curve of the 150 °C *h.p.* flake compared to its modelled and pristine curves at all excitation frequencies was observed, which confirmed OVD-induced manipulation in k_x and group velocities $v_{g,x} = \partial\omega/\partial k_x$. The v_g of the 150 °C *h.p.* flake was calculated to be $(v_{g,x})_{h.p.} \approx 1.39(v_{g,x})_{\text{pristine}}$. It must be noted that the $(v_{g,x})_{\text{pristine}} = 4.16 \times 10^{-3}c$, where c is the speed of light; see Supplementary Information, Note S3. A comparison of the group velocities extracted for pristine (purple) and 150 °C *h.p.* (green) flake is shown in Fig. 3g. Furthermore, the modulation in polariton wavelength of the *h.p.* flake was measured to be $(\lambda_p)_{h.p.} = 1.22(\lambda_p)_{\text{pristine}}$, respectively. Because of their increased v_g , *h.p.* flakes demonstrated a relatively smaller confinement factor across various excitation frequencies

compared to the pristine flakes. Based on the previously calculated HPhP propagation lengths, we calculated the polariton lifetimes $\tau = L/v_g$ of the pristine and *h.p.* flake across different frequencies, which has been presented in [Supporting Information, Note S4](#). At $\omega_0 = 901 \text{ cm}^{-1}$, the lifetimes were $0.92 \pm 0.06 \text{ ps}$ for pristine and $0.86 \pm 0.11 \text{ ps}$ for 150°C *h.p.* flake. Intriguingly, the loss in average τ of HPhPs in the 150°C *h.p.* flakes was only $6.52 \pm 0.12 \%$, which suggested low-loss HPhPs propagation in oxygen deficient $\alpha\text{-MoO}_3$. Comparing with the previous reports where the modulation in HPhPs has been attempted by modifying the crystallographic features in $\alpha\text{-MoO}_3$, the τ losses are much higher (30-45%).⁴⁶ Therefore, we believe that introduction of OVDs successfully modified the HPhP response without greatly reducing the HPhP lifetime. The FDTD calculated electric field profiles and their corresponding polariton lengths across various excitation frequencies has been presented in [Supporting Information, Fig. S9](#).

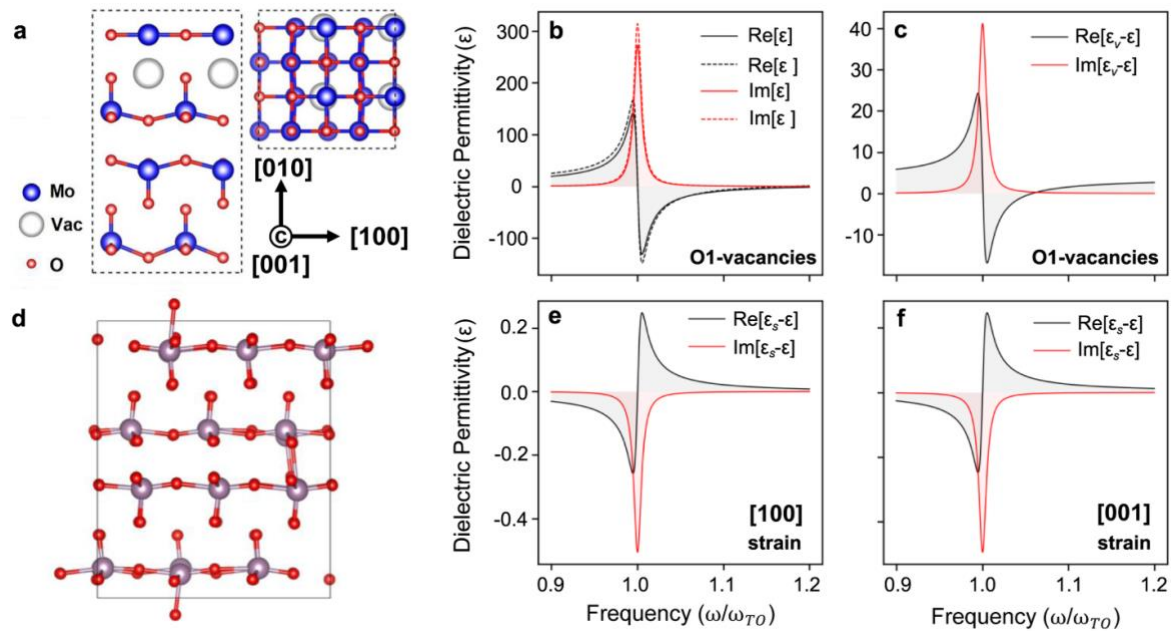


Figure 4: DFT calculations of OVDs-induced dielectric permittivity modulation in *h.p.* $\alpha\text{-MoO}_3$.

a Crystal structure of relaxed crystal structure of $\alpha\text{-MoO}_3$ with oxygen vacancies at the O1 site near van der Waals gap. **b** The corresponding IR dielectric response in the [100] direction, where solid

lines represent the dielectric of pristine α -MoO₃, and dashed lines correspond to that of the oxygen-deficient α -MoO₃. **c** The plot of difference between the dielectrics of the oxygen-deficient and pristine α -MoO₃. **d** Strained crystal lattice oxygen-deficient (O1 vacancies). **e-f** Variation in the dielectric response of α -MoO₃ under -2% compressive strain along [100] and [001], respectively. Dielectric functions have been plotted with respect to $(\omega/\omega_{\text{TO}})$, where ω_{TO} is the transverse optical mode of α -MoO₃ that is probed in this study.

DISCUSSION

OVDs are proposed as the main mechanism of HPhP dispersion modification. Our hypothesis is that their presence alternates the overall static polarizability of the crystal, having a profound impact on the dielectric permittivity of MoO_{3-x}, which, in turn, affects the optical response. DFT results yield static dielectric constants of 5.78, 4.33 and 6.47 for the [100], [010] and [001] crystallographic axes of pristine MoO₃ (Fig. 4a), consistent with that previously reported.⁴⁷ These values modify to 9.50, 4.81 and 9.36 for the defect geometry considered, where one of the O1 atoms is missing; see Fig. 4b. Significant increases of the static permittivity along [100] and [001] are attributed to the formation of the dipole moments at defect sites that enhance the dielectric screening capability of the material. This effect is much less significant in the [010] direction since the van der Waals gap limits interlayer interaction. The [100] transverse optical phonon mode of experimental interest (ω_{TO}) is calculated at 760 cm⁻¹, which is consistent with previous DFT results but differs from the experimental value of 819 cm⁻¹.⁴⁸ The discrepancy may be due to inherent limitations of the functional used or from the density of states considerations that are not accounted for in our analysis. By setting the Hubbard U value to 5 eV, we have achieved a defect structure that aligns well with previous calculations.⁴⁹ With the Hubbard U correction omitted, however, we observe a notable change in the converged geometry, yet the resulting dielectric response

is qualitatively similar. This suggests that the chosen value of the Hubbard U term does not significantly impact our findings.

Our DFT calculations (Fig. 4b; Supporting Information, Note S5) suggest that, due to the introduction of OVDs in *h.p.* flakes, the real part of the permittivity sees the corresponding reduction within the range from ω_{TO} to $\approx 1.05\omega_{\text{TO}}$, with $|\Delta\varepsilon/\varepsilon| \approx 0.1$, which is qualitatively agrees with the order of magnitude variation in ε extracted from the FDTD calculations and experiments. This behavior contrasts with the strain-induced permittivity, which only shows positive changes in ε within the Reststrahlen band, as seen in Fig 4e,f for the strain along [100] and [001], respectively. Thus, our calculations agree well with the OVD hypothesis of the observed changes of the dielectric permittivity and the HPhP dispersion tuning.

In summary, we have thermomechanically engineered the stoichiometry of $\alpha\text{-MoO}_3$ to control the dispersion of HPhPs. The introduction of controlled oxygen vacancy defects (OVDs) in hot-pressed $\alpha\text{-MoO}_3$, gradually alters its valence state from stoichiometric Mo^{6+} to non-stoichiometric Mo^{5+} , resulting in an increase in its static dielectric permittivity ε , as confirmed by our DFT calculations and FDTD simulations. As a result, the polariton wavelengths in the HPhPs dispersion of *h.p.* flakes increased by up to 19% within the frequency range of ω_0 from 880 to 920 cm^{-1} , as confirmed by our near-field experiments. This increased the polariton group velocity from $4.16 \times 10^{-3}c$ to $5.78 \times 10^{-3}c$ at $\omega_0 = 901 \text{ cm}^{-1}$, while the lifetimes showed a small loss of $\sim 7\%$. Our results suggest that hot-pressing-induced OVDs in $\alpha\text{-MoO}_3$ provides an excellent opportunity to manipulate mid-infrared HPhPs and can serve as a promising platform for next generation optical modulators, super-resolution imaging, enhanced molecular sensing, and on-chip optical communication.

METHODS

Thermomechanical Processing of α -MoO₃ flakes

Bulk vdW crystals of high-quality α -MoO₃ (2D Semiconductor Inc.) were mechanically exfoliated directly onto the precleaned and atomically flat (10×10 mm²) Si substrates (MTI Corp). The Si substrate capped with exfoliated samples was covered by another identical substrate to form a Si/ α -MoO₃/Si assembly. The assembly was then placed in a home-built pressure device to apply a mild uniaxial pressure onto the flakes while heating ([Supporting Information, Fig. S1b](#)). The overall pressure device assembly was then placed in a commercial benchtop muffle furnace (Thermo Scientific™) and heated at various temperatures in ambient conditions.

Raman Microscopy

A confocal Raman microscope (Renishaw Inc.), equipped with an objective lens (Nikon Plan Fluor 50 X, NA=0.4) and a 532 nm unpolarized laser source (22 mW, 50× objective, spot size 1 μ m) in ambient conditions was used to acquire micro-Raman and PL spectra of hot-pressed α -MoO₃ flakes lying on Si substrates. For Raman mapping, the smallest step size (100 nm) was used in both directions, while the spectrometer had a resolution of 0.5 cm⁻¹.

Structural and chemical characterizations

A Quanta™ 3D FIB-SEM was used to capture high-resolution Field Emission Scanning Electron Microscope (FESEM) images of pre- and post-processed α -MoO₃ flakes. A multipurpose JEOL-2800 transmission electron microscope with the resolution of 0.1 nm, operated at 200 to 80 kV, was used to perform energy dispersive spectroscopy (EDS). TEM samples were prepared by immersing and ultrasonically Si substrate capped with hot-pressed MoO₃ flakes in ethanol for 30 minutes. This isolated the flakes in ethanol yielded an MoO₃/ethanol dispersion, which was dropped onto the carbon-coated Cu grid by a micropipette to perform EDS characterization.

The X-ray photoelectron spectroscopy (XPS) was performed by using AXIS Supra by Kratos analytical instrument with a dual anode AlK α (1487.6/eV) monochromatic X-ray source, and high spatial resolution of 0.1 μm to characterize the chemical composition and stoichiometry of hot-pressed $\alpha\text{-MoO}_3$. The binding energy calibration was performed carefully by using C1s peak (284.8 eV) as a reference value.

PiFM measurements

A Molecular Vista Inc. VistaScope microscope was connected to a Block Engineering LaserTune quantum cascade laser (QCL) system, offering a wave number resolution of 0.5 cm^{-1} and a tunable range from 782 to 1920 cm^{-1} . During the operation, the microscope utilized NCH-PtIr 300 kHz cantilevers from Molecular Vista and operated in sideband mode at a QCL intensity of 5%.

Device Simulation

We performed full-wave electromagnetic simulations using a finite-difference time-domain (FDTD) method on commercially available Ansys Lumerical FDTD software. Individual $\alpha\text{-MoO}_3$ flakes with certain geometrical features on silicon substrates are investigated. The boundary conditions along the x -, y - and z -directions are set with perfectly matched layers. To excite and launch highly confined HPhPs, we use an electric dipole source. The dipole is polarized along the z -direction. We placed the dipole at 150 nm from the uppermost surface of the sample. The real part of E_z is monitored at 10 nm on top of the uppermost surface. The dispersion contours are then calculated by using these captured $\text{Re}(E_z)$ into a fast Fourier transform. Moreover, in our PiFM setup, the QCL uses a p -polarized light for illuminating the metal tip kept ~ 30 nm away from the top surface of the target flakes. As a result, the collected polaritonic electric fields are predominantly concentrated along the z -direction. Such a dipole excitation mechanism allows us to mimic the PiFM excitation and collection

scheme in a more realistic manner. The permittivity of the α -MoO₃ flakes has been obtained from previous reports.

DFT Calculations

DFT calculations were performed using the Vienna ab initio Simulation Package (VASP)⁵¹ with projector augmented wave (PAW) pseudopotentials Mo (4s2 4p6 5s1 4d5) and O (2s2 2p4).^{6,52} We took it further by employing the vdW-DF approach, which accounts for the intriguing dispersion interaction between the structure layers. Optimizing the unit cell with various exchange functionals paired with vdW-DF. To achieve impeccable precision, we pushed the boundaries, reaching convergence with an energy cutoff for the plane-wave basis set of an astounding 700 eV for 2×2×1 supercell, meticulously integrated with a 4×4×2 gamma-centered k-point grid for Brillouin zone exploration.⁵³ All structures were fully optimized until the residual forces on the ions were less than 0.01 eV for stoichiometric cells and a minuscule 0.05 eV for defect cells.⁵⁴

Author Contributions

N.H. and M.R.S conceived the idea and designed the experiments. N.H. fabricated and processed the samples and conducted material characterizations. Z.L. in consultation with H.K.W. performed PiFM measurements. M.A.S. in consultation of N.H. and M.R.S. performed PiFM data analysis. W.H., R.W. and A.S. performed DFT calculations. N.H. and M.A.S. drafted the manuscript. M.R.S. supervised the project. All authors contributed to the manuscript and approved its final version.

Acknowledgments

M.R.S. and W.H. acknowledge support from DARPA (grant #D22AP00153). This research was partially supported by the National Science Foundation Materials Research Science and

Engineering Center program through the UC Irvine Center for Complex and Active Materials (DMR-2011967). Micro-Raman and PL measurements were performed in UCI Laser Spectroscopy Laboratories.

References

- 1 Basov, D., Fogler, M. & García de Abajo, F. Polaritons in van der Waals materials. *Science* **354**, aag1992 (2016).
- 2 Dai, S. *et al.* Tunable phonon polaritons in atomically thin van der Waals crystals of boron nitride. *Science* **343**, 1125-1129 (2014).
- 3 Vakil, A. & Engheta, N. Transformation optics using graphene. *Science* **332**, 1291-1294 (2011).
- 4 Sun, Z., Martinez, A. & Wang, F. Optical modulators with 2D layered materials. *Nature Photonics* **10**, 227-238 (2016).
- 5 Li, P. *et al.* Hyperbolic phonon-polaritons in boron nitride for near-field optical imaging and focusing. *Nature Communications* **6**, 7507 (2015).
- 6 Wu, Y. *et al.* Chemical switching of low-loss phonon polaritons in α -MoO₃ by hydrogen intercalation. *Nature Communications* **11**, 2646 (2020).
- 7 Shelby, R. A., Smith, D. R. & Schultz, S. Experimental verification of a negative index of refraction. *Science* **292**, 77-79 (2001).
- 8 Tsakmakidis, K. L., Boardman, A. D. & Hess, O. 'Trapped rainbow' storage of light in metamaterials. *Nature* **450**, 397-401 (2007).
- 9 Poddubny, A., Iorsh, I., Belov, P. & Kivshar, Y. Hyperbolic metamaterials. *Nature Photonics* **7**, 948-957 (2013).
- 10 Cubukcu, E., Aydin, K., Ozbay, E., Foteinopoulou, S. & Soukoulis, C. M. Negative refraction by photonic crystals. *Nature* **423**, 604-605 (2003).

- 11 Parimi, P. V., Lu, W. T., Vodo, P. & Sridhar, S. Imaging by flat lens using negative refraction. *Nature* **426**, 404-404 (2003).
- 12 Huang, K. C., Bienstman, P., Joannopoulos, J. D., Nelson, K. A. & Fan, S. Field expulsion and reconfiguration in polaritonic photonic crystals. *Physical Review Letters* **90**, 196402 (2003).
- 13 Chaudhary, K. *et al.* Engineering phonon polaritons in van der Waals heterostructures to enhance in-plane optical anisotropy. *Science Advances* **5**, eaau7171 (2019).
- 14 Dubrovkin, A. M., Qiang, B., Krishnamoorthy, H. N., Zheludev, N. I. & Wang, Q. J. Ultra-confined surface phonon polaritons in molecular layers of van der Waals dielectrics. *Nature Communications* **9**, 1762 (2018).
- 15 Folland, T. G. *et al.* Reconfigurable infrared hyperbolic metasurfaces using phase change materials. *Nature Communications* **9**, 4371 (2018).
- 16 Fali, A. *et al.* Refractive index-based control of hyperbolic phonon-polariton propagation. *Nano Letters* **19**, 7725-7734 (2019).
- 17 Dai, S. *et al.* Phase-change hyperbolic heterostructures for nanopolaritonics: a case study of hBN/VO₂. *Advanced Materials* **31**, 1900251 (2019).
- 18 Dai, S. *et al.* Hyperbolic phonon polaritons in suspended hexagonal boron nitride. *Nano Letters* **19**, 1009-1014 (2018).
- 19 Hu, H. *et al.* Gate-tunable negative refraction of mid-infrared polaritons. *Science* **379**, 558-561 (2023).
- 20 Zhang, Q. *et al.* Interface nano-optics with van der Waals polaritons. *Nature* **597**, 187-195 (2021).
- 21 Ma, W. *et al.* In-plane anisotropic and ultra-low-loss polaritons in a natural van der Waals crystal. *Nature* **562**, 557-562 (2018).

- 22 Wang, M. & Koski, K. J. Reversible chemochromic MoO₃ nanoribbons through zerovalent metal intercalation. *ACS Nano* **9**, 3226-3233 (2015).
- 23 Zheng, Z. *et al.* Highly confined and tunable hyperbolic phonon polaritons in van der Waals semiconducting transition metal oxides. *Advanced Materials* **30**, 1705318 (2018).
- 24 De Castro, I. A. *et al.* Molybdenum oxides—from fundamentals to functionality. *Advanced Materials* **29**, 1701619 (2017).
- 25 Hussain, N. *et al.* Quantum-confined blue photoemission in strain-engineered few-atomic-layer 2D germanium. *Nano Energy* **83**, 105790 (2021).
- 26 Hussain, N. *et al.* Ultra-Narrow Linewidth Photo-Emitters in Polymorphic Selenium Nanoflakes. *Small*, 2204302 (2022).
- 27 Illyaskutty, N. *et al.* Alteration of architecture of MoO₃ nanostructures on arbitrary substrates: growth kinetics, spectroscopic and gas sensing properties. *Nanoscale* **6**, 13882-13894 (2014).
- 28 Mestl, G., Verbruggen, N., Bosch, E. & Knözinger, H. Mechanically activated MoO₃. 5. Redox behavior. *Langmuir* **12**, 2961-2968 (1996).
- 29 Liu, H. *et al.* Huge Absorption Edge Blue shifts of Layered α -MoO₃ Crystals upon Thickness Reduction Approaching 2D Nanosheets. *The Journal of Physical Chemistry C* **122**, 12122-12130 (2018).
- 30 de Castro Silva, I., Reinaldo, A. C., Sigoli, F. A. & Mazali, I. O. Raman spectroscopy-in situ characterization of reversibly intercalated oxygen vacancies in α -MoO₃. *RSC Advances* **10**, 18512-18518 (2020).
- 31 Py, M. & Maschke, K. Intra-and interlayer contributions to the lattice vibrations in MoO₃. *Physica B+ C* **105**, 370-374 (1981).

- 32 Alsaif, M. M. *et al.* Tunable plasmon resonances in two-dimensional molybdenum oxide nanoflakes. *Advanced Materials* **26**, 3931-3937 (2014).
- 33 Aschauer, U. *et al.* Strain-controlled oxygen vacancy formation and ordering in CaMnO_3 . *Physical Review B* **88**, 054111 (2013).
- 34 Chandrasena, R. U. *et al.* Strain-engineered oxygen vacancies in CaMnO_3 thin films. *Nano Letters* **17**, 794-799 (2017).
- 35 Swiatowska-Mrowiecka, J. *et al.* Li-ion intercalation in thermal oxide thin films of MoO_3 as studied by XPS, RBS, and NRA. *The Journal of Physical Chemistry C* **112**, 11050-11058 (2008).
- 36 Dieterle, M., Weinberg, G. & Mestl, G. Raman spectroscopy of molybdenum oxides Part I. Structural characterization of oxygen defects in MoO_{3-x} by DR UV/VIS, Raman spectroscopy and X-ray diffraction. *Physical Chemistry Chemical Physics* **4**, 812-821 (2002).
- 37 Wang, G., Ling, Y. & Li, Y. Oxygen-deficient metal oxide nanostructures for photoelectrochemical water oxidation and other applications. *Nanoscale* **4**, 6682-6691 (2012).
- 38 Kim, H.-S. *et al.* Oxygen vacancies enhance pseudocapacitive charge storage properties of MoO_{3-x} . *Nature Materials* **16**, 454-460 (2017).
- 39 Zhang, Y. *et al.* High-capacity and kinetically accelerated lithium storage in MoO_3 enabled by oxygen vacancies and heterostructure. *Advanced Energy Materials* **11**, 2101712 (2021).
- 40 Wuttig, M. *et al.* The role of vacancies and local distortions in the design of new phase-change materials. *Nature Materials* **6**, 122-128 (2007).

- 41 Caravati, S., Bernasconi, M., Kühne, T., Krack, M. & Parrinello, M. Coexistence of tetrahedral-and octahedral-like sites in amorphous phase change materials. *Applied Physics Letters* **91** (2007).
- 42 Deringer, V. L., Tchougréeff, A. L. & Dronskowski, R. Crystal orbital Hamilton population (COHP) analysis as projected from plane-wave basis sets. *The Journal of Physical Chemistry A* **115**, 5461-5466 (2011).
- 43 Maintz, S., Deringer, V., Tchougréeff, A. & Dronskowski, R. The mathematical apparatus and the framework on which LOBSTER is built. *J. Comput. Chem* **34**, 2557-2567 (2013).
- 44 Tamagnone, M. *et al.* Ultra-confined mid-infrared resonant phonon polaritons in van der Waals nanostructures. *Science Advances* **4**, eaat7189 (2018).
- 45 Nowak, D. *et al.* Nanoscale chemical imaging by photoinduced force microscopy. *Science Advances* **2**, e1501571 (2016).
- 46 Taboada-Gutiérrez, J. *et al.* Broad spectral tuning of ultra-low-loss polaritons in a van der Waals crystal by intercalation. *Nature Materials* **19**, 964-968 (2020).
- 47 Lajaunie, L., Boucher, F., Dessapt, R. & Moreau, P. Strong anisotropic influence of local-field effects on the dielectric response of α -MoO₃. *Physical Review B* **88**, 115141 (2013).
- 48 Tong, Z., Dumitrică, T. & Frauenheim, T. First-principles prediction of infrared phonon and dielectric function in biaxial hyperbolic van der Waals crystal α -MoO₃. *Physical Chemistry Chemical Physics* **23**, 19627-19635 (2021).
- 49 Inzani, K., Grande, T., Vullum-Bruer, F. & Selbach, S. M. A van der Waals density functional study of MoO₃ and its oxygen vacancies. *The Journal of Physical Chemistry C* **120**, 8959-8968 (2016).

- 50 Álvarez-Pérez, G. *et al.* Infrared permittivity of the biaxial van der waals semiconductor α -MoO₃ from near-and far-field correlative studies. *Advanced Materials* **32**, 1908176 (2020).
- 51 Kresse, G. & Hafner, J. Ab initio molecular dynamics for liquid metals. *Physical Review B* **47**, 558 (1993).
- 52 Blöchl, P. E. Projector augmented-wave method. *Physical review B* **50**, 17953 (1994).
- 53 Monkhorst, H. J. & Pack, J. D. Special points for Brillouin-zone integrations. *Physical Review B* **13**, 5188 (1976).
- 54 Kresse, G. & Furthmüller, J. Efficient iterative schemes for ab initio total-energy calculations using a plane-wave basis set. *Physical Review B* **54**, 11169 (1996).

Vacancy-Engineered Phonon Polaritons in α -MoO₃.

Supporting Information

Naveed Hussain,¹ Mashnoon Alam Sakib,¹ Zhaoxu Li,² William Harris,^{1,3} Shehzad Ahmed,⁴
Ruqian Wu,³ H. Kumar Wickramasinghe,^{1,2} Maxim R. Shcherbakov*^{1,2,5}

¹*Department of Electrical Engineering and Computer Science, University of California, Irvine, CA 92697*

²*Department of Materials Science and Engineering, University of California, Irvine, CA 92697*

³*Department of Physics, University of California, Irvine, CA 92697*

⁴*State Key Laboratory for Mechanical Behavior of Materials, Xi'an Jiaotong University, Xi'an 710049, China*

⁵*Beckman Laser Institute and Medical Clinic, University of California, Irvine, CA 92697*

Table of Contents:

Note S1. Molecular structure of α -MoO₃ and the creation of OVDs

Note S2. Modeling the permittivity of α -MoO₃

Note S3. Extraction of group velocities of α -MoO₃ HPhPs

Note S4. Lifetimes calculations of HPhPs in α -MoO₃

Note S5. DFT calculations of Dielectric function

Note S6. Pressure calculations

Fig. S1. a FESEM image of an exfoliated α -MoO₃ flake. **b** Pressure device assembly is made of two stainless steel bars, which is used to apply mild uniaxial pressure while subsequently heated in a muffle furnace. **c** Hot-pressed flake with its crystal orientation. The scale bar in b and c is 10 μ m.

Fig. S2. a Comparison of FWHM (Γ) of A_g/B_{1g} phonon mode of pristine, and h.p. α - MoO_3 at 150 and 350 °C. The increase in FWHM with increase in h.p. temperature indicates the introduction of vacancy defect states in α - MoO_3 .

Fig. S3. a blue shift in T_b (A_g/B_{1g}) (translational chain) mode with h.p. temperature, showing lattice strain engineering. **b** Comparison of compressive strain induction in just heated and h.p. flakes with temperature, and their respective strain release (slippage) points.

Fig. S4. X-ray photoelectron spectroscopy (XPS) survey spectrum of h.p. α - MoO_3 at 350 °C on gold-coated substrate.

Fig. S6. Elemental Dispersive Spectroscopy (EDS) of α - MoO_3 h.p. at 350 °C. **a** TEM image of the flake. **b-c** elemental mapping of Mo and O₂ collected from an area highlighted in a. **d** Elemental intensity profile of mapping.

Fig. S6. a-b Crystal structure of pristine and relaxed crystal structure of α - MoO_3 with oxygen vacancies near van der Waals gap. **c-e** Total density of states of pristine (a) and defected α - MoO_3 with the increase in oxygen vacancies in MoO_{3-x} crystal structures (d and e).

Fig. S7. a-b Atomic force microscopy (AFM) image and corresponding height profile (across the blue line) of pristine α - MoO_3 flake. **c-d** AFM image and corresponding height profile of h.p. flake.

Fig. S8. The real and imaginary components of the IR dielectric permittivity of α - MoO_3 along the three crystallographic axes. The crystallographic axes: [001], [100] and [010], correspond to phonons on each of the Reststrahlen bands (RB_1 , RB_2 and RB_3), respectively.

Fig. S9. FDTD simulation. a Electric field distributions across different excitation frequencies. **b** Line traces of the real part of the electric field along the z-direction. The field profiles and line traces are calculated for different frequencies (880 - 920 cm^{-1}) along the [100] direction of the pristine α - MoO_3 flake ($d = 107.5$ nm).

Note S1: Molecular structure of α -MoO₃ and the creation of OVDs.

Understanding the role of inter- and intralayer contributions to lattice vibrations (phonons) in α -MoO₃ is critical for determining which site contributes the most to thermally generated OVDs. The O1 is often termed as the terminal oxygen (t-O₁) owing to its proximity to the vdW gaps along the z-axis and is governed by the interlayer coupling. The stretching force constants (f_{16} and f_{17}) of interlayer coupling are $f_{16} = 9.3$ N/m, and $f_{17} = 2$ N/m, which are considerably lower as compared to the force constants along the interchain ($f_4 = f_5 = 80$ N/m) and intrachain ($f_1 = 791.5$, $f_2 = 466$ and $f_3 = 171$ N/m) directions. Furthermore, the bond lengths corresponding to f_{16} and f_{17} are 2.82 and 3.24 Å, respectively, are larger those of along the inter- and intrachain directions.^{S1}

Note S2: Modeling the permittivity of α -MoO₃.

Since α -MoO₃ is an anisotropic polar dielectric crystal, we model the permittivity by the Lorentz model for the case of coupled oscillators (also known as the TO-LO model).^{S2,S3} We use three oscillators for approximating ε_x and one oscillator each for the cases of ε_y and ε_z , respectively.

$$\varepsilon_x(\omega) = \varepsilon_x^\infty \left(\frac{(\omega_{x1}^{LO})^2 - \omega^2 - i\gamma_{x1}\omega}{(\omega_{x1}^{TO})^2 - \omega^2 - i\gamma_{x1}\omega} \right) \left(\frac{(\omega_{x2}^{LO})^2 - \omega^2 - i\gamma_{x2}\omega}{(\omega_{x2}^{TO})^2 - \omega^2 - i\gamma_{x2}\omega} \right) \left(\frac{(\omega_{x3}^{LO})^2 - \omega^2 - i\gamma_{x3}\omega}{(\omega_{x3}^{TO})^2 - \omega^2 - i\gamma_{x3}\omega} \right),$$
$$\varepsilon_y(\omega) = \varepsilon_y^\infty \left(\frac{(\omega_{y1}^{LO})^2 - \omega^2 - i\gamma_{y1}\omega}{(\omega_{y1}^{TO})^2 - \omega^2 - i\gamma_{y1}\omega} \right),$$
$$\varepsilon_z(\omega) = \varepsilon_z^\infty \left(\frac{(\omega_{z1}^{LO})^2 - \omega^2 - i\gamma_{z1}\omega}{(\omega_{z1}^{TO})^2 - \omega^2 - i\gamma_{z1}\omega} \right),$$

In this Lorentz model, the three principal axes of the α -MoO₃ can be considered in the [100], [001] and [010] directions. Here, the $\varepsilon_x(\omega)$, $\varepsilon_y(\omega)$, and $\varepsilon_z(\omega)$ represent the three principal components of the permittivity tensor, respectively. To generalize this representation, the permittivity tensors can be then denoted by $\varepsilon_i(\omega)$ where the $i = x, y, z$. Here, the static

dielectric constant is represented by ε_i^∞ . The LO and TO phonon frequencies along the three directions is represented by ω_{ij}^{LO} and ω_{ij}^{TO} along the i -th direction with $i = x, y, z$ respectively. Moreover, γ_{ij} represent the damping factor of the Lorentzian line shape derived from the phonon scattering rate. The subscript j here represents the different phonon pairs along the same axis. The parameters used in modeling the dielectric permittivity model of the α -MoO₃ system have been utilized by model fitting the optical response of the material measured from polarized far-field IR spectroscopy.^{S2} The static dielectric permittivity tensor components are taken as $\varepsilon_x^\infty = 5.78$, $\varepsilon_y^\infty = 6.07$, and $\varepsilon_z^\infty = 4.47$.

Table S1. Parameters of the Lorentz model of MoO₃ dielectric permittivity.

Main axis (i)	Mode index (j)	ω_{ij}^{TO} , cm ⁻¹	ω_{ij}^{LO} , cm ⁻¹	γ_{ij} , cm ⁻¹
x	1	506.7	534.3	49.1
x	2	821.4	963.0	6.0
x	3	998.7	999.2	0.35
y	1	544.6	850.1	9.5
z	1	956.7	1006.9	1.5

Our DFT calculations for OVD hypothesis reflect a significant increase in the static dielectric constants for a hot-pressed flake. To corroborate this defect geometry into our FDTD calculation, an anisotropic index modulation has been introduced. Here, the static dielectric permittivity tensor components, ε_x^∞ and ε_y^∞ , along the [100] and [001] directions, respectively; are adjusted to approximately fit the 150°C hot-pressed dispersion relation. For this case, the static dielectric constants are used as, $\varepsilon_x^\infty(h.p.) = 1.35$ $\varepsilon_x^\infty = 7.803$ and $\varepsilon_y^\infty(h.p.) = 1.35$ $\varepsilon_y^\infty = 8.1945$. Due to insignificant changes found in the DFT calculations along the [001] direction, the static dielectric constant ε_z^∞ was kept unchanged.

Note S3: Extraction of the α -MoO₃ HPhP group velocities.

Group velocity is defined by $v_g = \frac{\partial \omega}{\partial k_x}$. In order to calculate the group velocity of the α -MoO₃ PhPs, we use the first-order derivative of the dispersion curves $\omega(k_x)$ in Fig.3b (main text) which we get from the experimental PiFM measurements. We take the derivative along the [100] crystal axis directions since our frequency range of interest lies in the lower-Reststrahlen band (L-RB). For this, we numerically fit the experimental dispersion curve data points by a general potential function. This function is taken to be of $y = ax^b$. Followed by the fitting, in order to get the v_g , we then calculate a numerical derivative of the resulting curves.

Note S4: HPhPs Lifetime Calculations in α -MoO₃.

We performed the lifetime calculation of α -MoO₃ HPhPs according to $\tau_x = L_x/v_g$. Here, the group velocity is calculated from the experimentally recorded dispersion curves as mentioned in Fig.3b (main text). Moreover, for extracting the decay length L_x , we fitted the near-field line profile of the PhPs. This is essentially the real part of the z-component of the electric fields along the crystal direction of [100]. We fitted the captured PiFM signal to an exponentially decaying sinusoidal signal along with a dissipation factor. As the HPhPs start to propagate across the distance x , the field starts to decay exponentially. The model equation upon which we performed our fitting is mentioned below:

$$y = y_0 + Ae^{-\left(\frac{x}{t_0}\right)} \sin \left[\pi \left(\frac{x - x_c}{w} \right) \right],$$

where $A > 0$, $w > 0$ and $t_0 > 0$. For the fitting procedure, we used the Levenberg-Marquardt iteration algorithm until a preset amount of convergence ($\Delta\chi^2 < 10^{-9}$) was achieved. After the fitting is performed, we can calculate from the fitted parameter the desired propagation length which is in this case estimated as t_0 .

Note S5: DFT Calculations of the Dielectric Permittivity

DFT calculations were carried out using the Vienna ab initio Simulation Package (VASP) with projector augmented wave (PAW) pseudopotentials Mo_h and O_{sv} . The van der Waals dispersion interaction was accounted for using the semi-empirical DFT-D2 method implemented in VASP.^{S4} Calculations were performed with a plane-wave energy cutoff of 810 eV and with a Monkhorst-Pack k-point sampling of $9 \times 2 \times 9$ for the pristine geometry and $3 \times 2 \times 3$ for the $3 \times 1 \times 3$ defected supercell. We further implement the Dudarev DFT+U method to treat the Mo 4d orbitals of Mo ($U = 5\text{eV}$).^{S5} Forces were converged to less than $0.01 \text{ eV}/\text{\AA}$ for all structures and to less than $0.005 \text{ eV}/\text{\AA}$ for phonon calculations. The phonon frequencies and eigen modes were obtained through finite difference using the Phonopy package.^{S6,S7}

For the defect geometry, we consider the O1 vacancy position, which was previously identified as the lowest energy vacancy configuration of MoO_3 .^{S8} The method for obtaining the dielectric function of pristine MoO_3 follows a similar procedure to that outlined in previous studies.^{S9} For strained and defect geometries, however, we find approximate dielectric permittivities using the same eigenmodes and frequencies found from the pristine structure, while updating the static dielectric constant and born effective charges (averaged down to a $1 \times 1 \times 1$ cell in the case of the vacancy geometry). This way, we avoid the expense of large phonon calculations while capturing the main physics in the limit of small variation away from pristine MoO_3 .

Note S6: Pressure calculations.

We estimate the pressure exerted on the sample with the PDA using the following expression:

$$\sigma = G \left[\frac{4\Delta x}{l} \right],$$

Where $G = 160$ GPa, is the bulk modulus of stainless steel, $\Delta x = 0.03$ cm is the shear on each side of steel bar, $l = 4$ cm is the half length of the steel bar. The estimated pressure is therefore $\sigma = 0.16$ GPa.

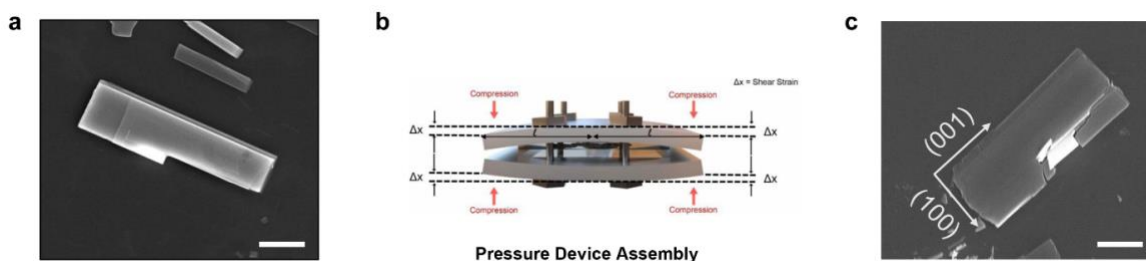


Fig. S1. **a** FESEM image of an exfoliated α -MoO₃ flake. **b** The pressure device assembly consists of a pair of stainless steel bars designed for the application of gentle uniaxial pressure, followed by heating in a muffle furnace. **c** Hot-pressed flake with its crystal orientation. The scale bar in **b** and **c** is 10 μ m.

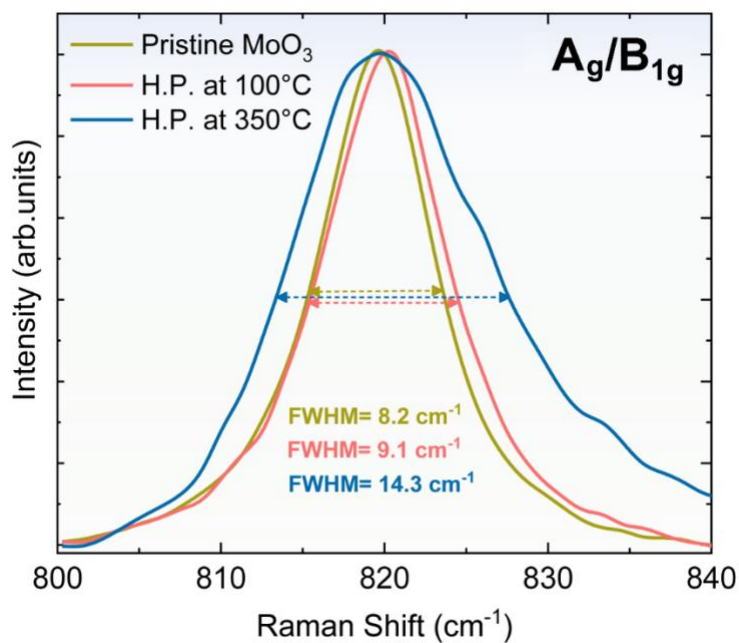


Fig. S2. Comparison of the FWHMs (Γ) of A_g/B_{1g} phonon mode of pristine and h.p. α -MoO₃ at 150 and 350°C. The increase in FWHM with increase in *h.p.* temperature indicates the introduction of vacancy defect states in α -MoO₃.

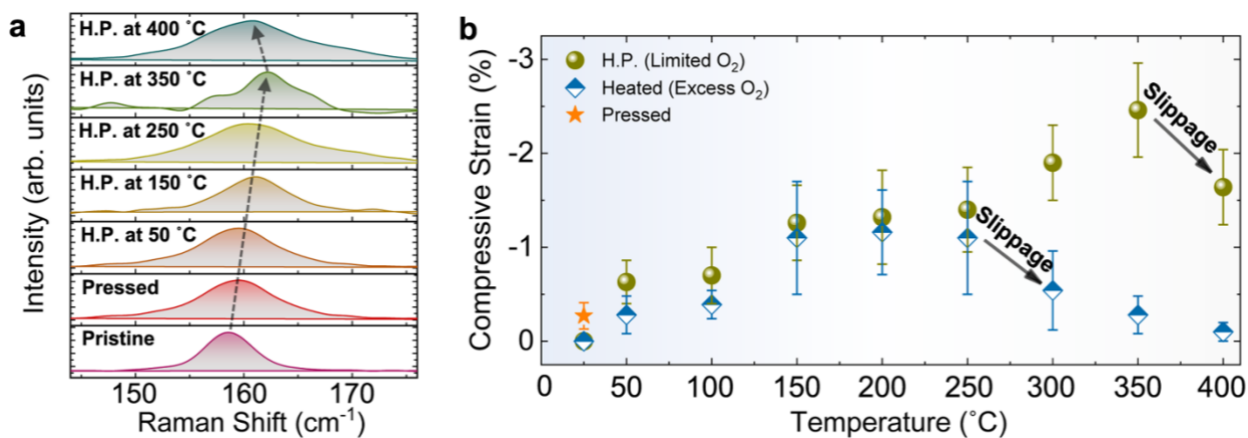


Fig. S3. a, Blue shift in T_b (A_g/B_{1g}) (translational chain) mode with h.p. temperature, showing lattice strain engineering. **b**, Comparison of compressive strain induction in just heated and h.p. flakes with temperature, and their respective strain release (slippage) points.

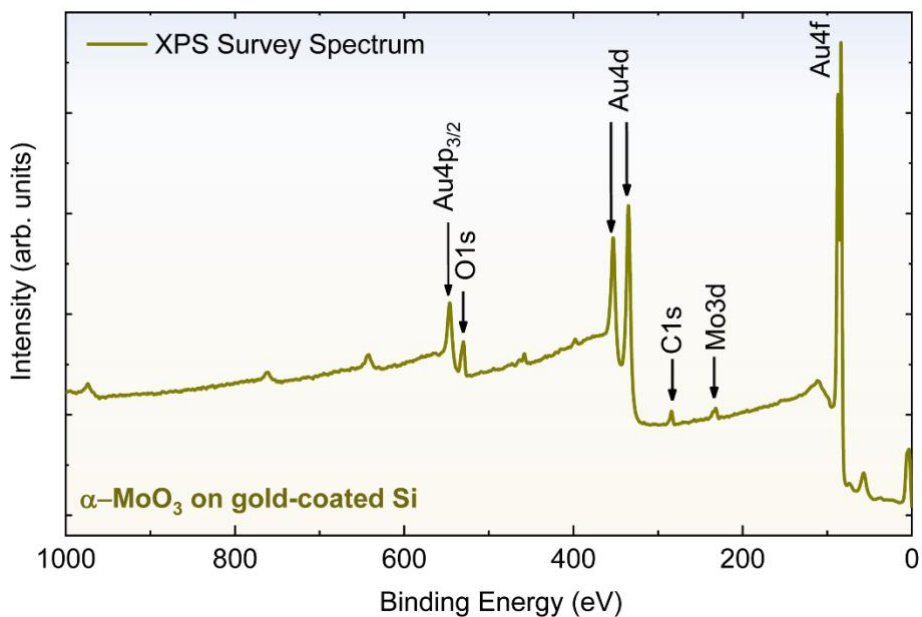


Fig. S4. X-ray photoelectron spectroscopy (XPS) survey spectrum of h.p. α -MoO₃ at 350 °C on gold-coated substrate.

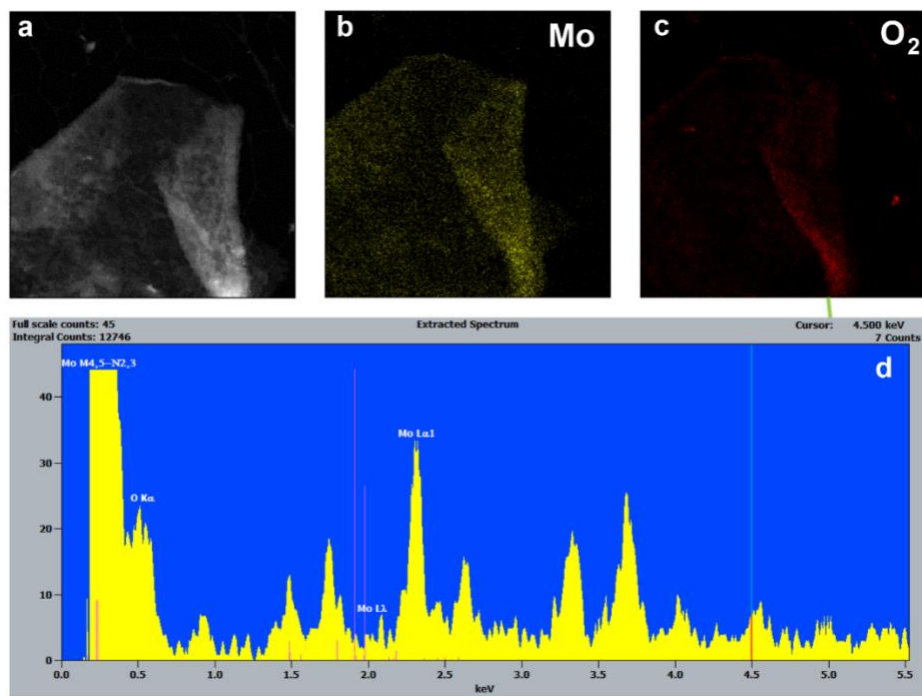


Fig. S5. Elemental Dispersive Spectroscopy (EDS) of α - MoO_3 *h.p.* at 350°C. **a** TEM image of the flake. **b-c** elemental mapping of Mo and O_2 collected from an area highlighted in a. **d** Elemental intensity profile of mapping.

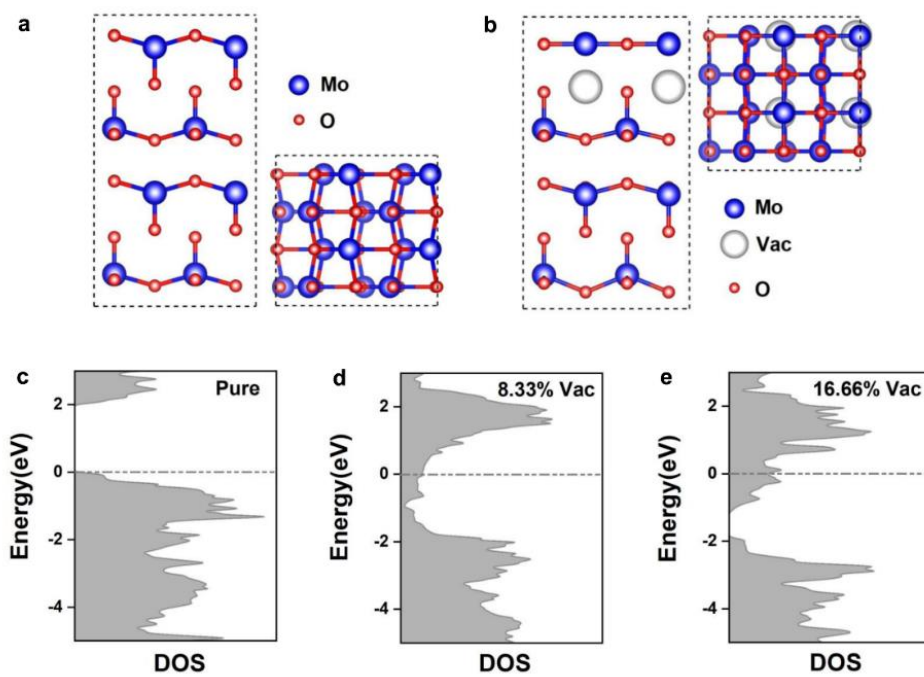


Fig. S6. **a-b** Crystal structure of pristine and relaxed crystal structure of α - MoO_3 with oxygen vacancies near van der Waals gap. **c-e** Total density of states of pristine (a) and defected α - MoO_3 with the increase in oxygen vacancies in MoO_{3-x} crystal structures (d and e).

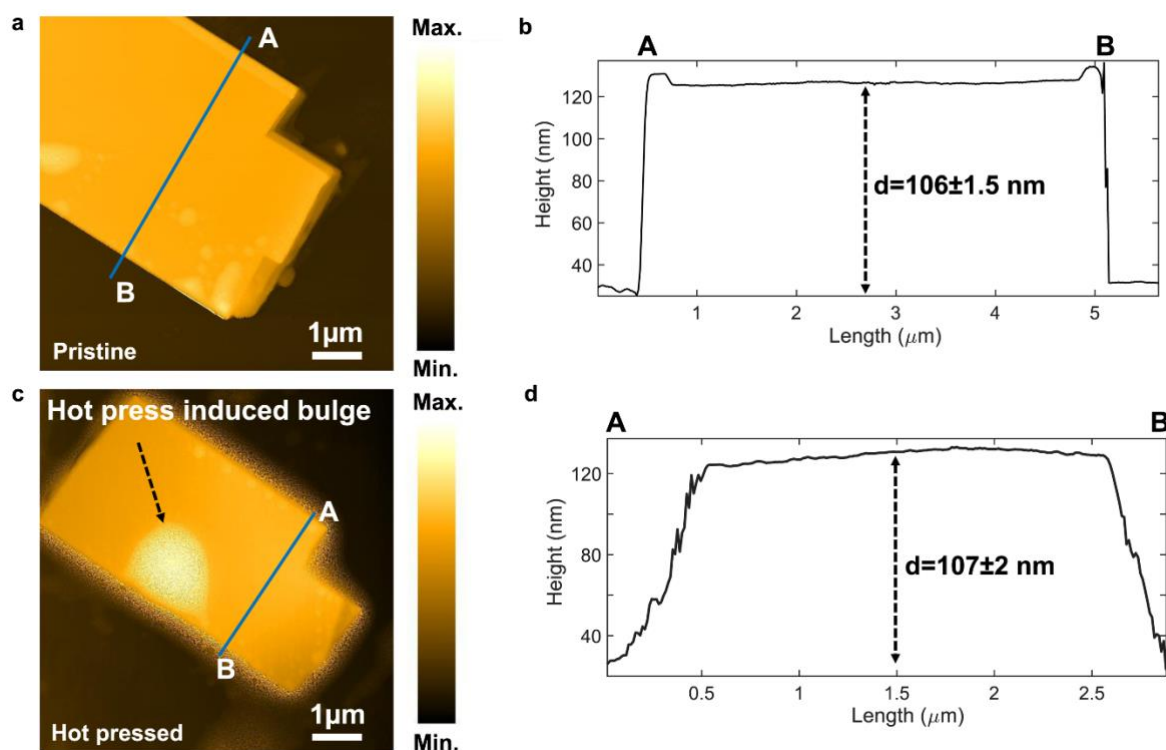


Fig. S7. **a-b** Atomic force microscopy (AFM) image and corresponding height profile (across the blue line) of pristine α - MoO_3 flake. **c-d** AFM image and corresponding height profile of h.p. flake.

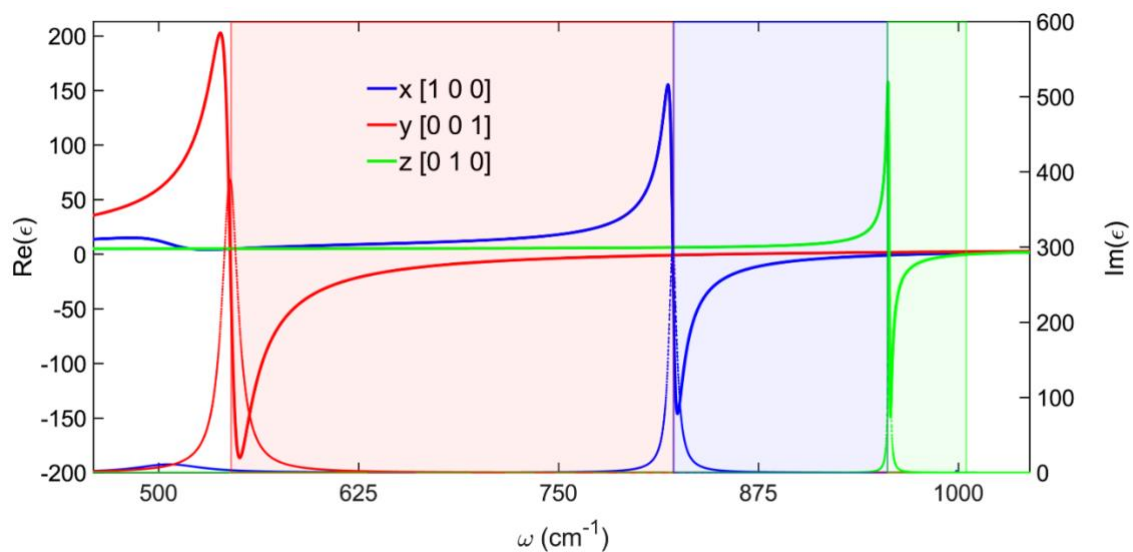


Fig. S8. The real and imaginary components of the dielectric permittivity of α - MoO_3 along the three crystallographic axes. The crystallographic axes: $[001]$, $[100]$ and $[010]$, correspond to phonons in each of the Reststrahlen bands (RB_1 , RB_2 and RB_3), respectively.

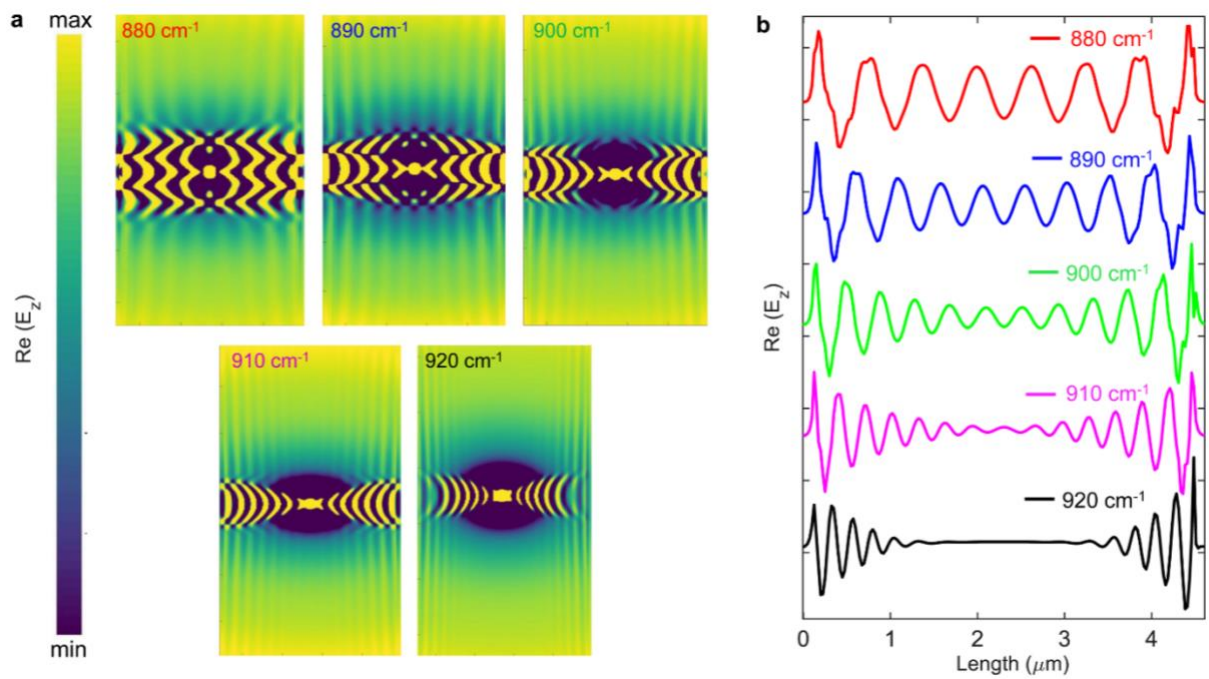


Fig. S9. FDTD simulations. **a** Electric field distributions across different excitation frequencies. **b** Line sections of the E_z real part maps. The field profiles and line traces are calculated for different frequencies (880 – 920 cm^{-1}) along the [100] direction of the pristine $\alpha\text{-MoO}_3$ flake ($d = 107.5$ nm).

References

- S1 Py, M. & Maschke, K. Intra- and interlayer contributions to the lattice vibrations in MoO_3 . *Physica B+C* **105**, 370-374 (1981).
- S2 Álvarez-Pérez, G. *et al.* Infrared permittivity of the biaxial van der Waals semiconductor $\alpha\text{-MoO}_3$ from near- and far-field correlative studies. *Advanced Materials* **32**, 1908176 (2020).
- S3 Folland, T., Nordin, L., Wasserman, D. & Caldwell, J. Probing polaritons in the mid- to far-infrared. *Journal of applied physics* **125** (2019).

- S4 Grimme, S. Semiempirical GGA-type density functional constructed with a long-range dispersion correction. *Journal of Computational Chemistry* **27**, 1787-1799 (2006).
- S5 Dudarev, S. L., Botton, G. A., Savrasov, S. Y., Humphreys, C. & Sutton, A. P. Electron-energy-loss spectra and the structural stability of nickel oxide: An LSDA+U study. *Physical Review B* **57**, 1505 (1998).
- S6 Togo, A., Chaput, L., Tadano, T. & Tanaka, I. Implementation strategies in phonopy and phono3py. *Journal of Physics: Condensed Matter* (2023).
- S7 Togo, A. First-principles phonon calculations with phonopy and phono3py. *Journal of the Physical Society of Japan* **92**, 012001 (2023).
- S8 Inzani, K., Grande, T., Vullum-Bruer, F. & Selbach, S. M. A van der Waals density functional study of MoO₃ and its oxygen vacancies. *The Journal of Physical Chemistry C* **120**, 8959-8968 (2016).
- S9 Tong, Z., Dumitrică, T. & Frauenheim, T. First-principles prediction of infrared phonon and dielectric function in biaxial hyperbolic van der Waals crystal α -MoO₃. *Physical Chemistry Chemical Physics* **23**, 19627-19635 (2021).